

# Probing the Mechanism of Selective Phosphate Adsorption from Wastewater using Aqueous and Synchrotron X-ray Characterization

Neha Sharma<sup>‡,a,c</sup>, Edward Apraku<sup>‡,b</sup>, Hannah E. Holmes<sup>‡,a</sup>, Meili Gong<sup>a</sup>, Diego Bustamante<sup>a</sup>, Johanna Nelson Weker<sup>c</sup>, Sharon Bone<sup>c</sup>, William Tarpeh<sup>\*,a,b</sup>

<sup>‡</sup>denotes equal contribution

<sup>\*</sup>denotes corresponding author

a) Department of Chemical Engineering, Stanford University, Stanford, CA, USA

b) Department of Civil and Environmental Engineering, Stanford University, Stanford, CA, USA

c) Stanford Synchrotron Radiation Lightsource, SLAC National Accelerator Laboratory, Menlo Park, CA, USA

**KEYWORDS:** *Nutrient recovery, phosphate recovery, adsorption, ion exchange, resins, synchrotron, radiography,  $\mu$ -XRF,  $\mu$ -XANES*

---

**ABSTRACT:** Ion exchange shows promise for recovering phosphate from wastewater as value-added products, but requires high phosphate selectivity to compete with conventional treatment. Hybrid anion exchange (HAIX) resins, which contain non-selective basic functional groups and selective iron oxide nanoparticles (FeOnp), can effectively remove phosphate from wastewater. However, knowledge gaps remain regarding the mechanisms of phosphate selectivity and influence of competing ions, hindering needed efforts to model adsorption dynamics and design scalable adsorption processes for varying wastewaters. To address these gaps, we integrated aqueous-phase adsorption analysis with solid-phase, synchrotron-based X-ray characterization; this integration facilitated elucidation of the distribution and speciation of iron, phosphate, and competing anions on HAIX resins. We compared a quaternary ammonium-functionalized HAIX resin (SBA) to a tertiary amine version (WBA) to determine the role of functional groups. X-ray radiography revealed differences in FeOnp speciation (goethite vs. ferrihydrite) and distribution (peripheral vs. homogeneous) between the resins, resulting in varied phosphate affinity and intraparticle diffusion resistance. Using micro-X-ray fluorescence ( $\mu$ -XRF) and micro-X-ray absorption near-edge structure ( $\mu$ -XANES) spectroscopy, we identified differences in where and how phosphate binds across resin types and wastewaters. Across wastewater compositions, FeOnp sites in WBA contribute more to phosphate adsorption than in SBA, possibly due to variations in Fe distribution and speciation. Phosphate adsorption densities calculated from quantitative  $\mu$ -XRF maps matched those from aqueous analysis, demonstrating the effectiveness of this integrated approach. Overall, results demonstrate the use of synchrotron-based X-ray characterization for investigating adsorption mechanisms and advance HAIX as a phosphate recovery technology from complex wastewaters.

---

## Introduction

Phosphorus is a key component of agricultural fertilizer but faces environmental and scarcity challenges stemming from mining phosphate rock. Fluctuations in phosphate content, impurities, and limited accessibility to phosphate reserves have decreased mineral quality and increased mining costs.<sup>1,2</sup> Globally over 220 million metric tons (MMTs) of phosphate rock are mined annually,<sup>3</sup> and 80% of the mined phosphorus is used for fertilizers. However, less than 40% of the phosphorus in applied fertilizers is taken up by plants,<sup>4,5</sup> and the excess phosphorus in field runoff contributes to eutrophication and harmful algal blooms. Phosphate recovery from wastewater provides an opportunity to circularize existing linear phosphorus management and offset dependence on phosphate rock. For example, over 3.6 MMTs of phosphate can theoretically be recovered from municipal wastewater,<sup>6</sup> with additional phosphate potentially recovered from agricultural runoff (**Figure S1**).

Conventional phosphate management techniques (e.g., adsorption, biological treatment, chemical precipitation) from waste sources (e.g., municipal wastewater, corn refineries) prioritize removal over recovery to meet the strict discharge requirements of wastewater treatment plants (WWTPs).<sup>7–10</sup> Additionally, established phosphate recycling practices apply sludge biosolids as a fertilizer and soil conditioner in agriculture. However, phosphate recycling from biosolids presents significant challenges, including the presence of hazardous substances (e.g., pathogens, heavy metals, and organic micropollutants), limited phosphorus bioavailability for plant uptake, and low product purity due to low phosphorus selectivity.<sup>11</sup>

Selective adsorbents provide an effective approach to wastewater phosphorus management, enabling both efficient phosphate removal and recovery of high-purity phosphate products via chemical regeneration. Specifically, hybrid anion exchange resins (HAIX) (crosslinked polystyrene containing quaternary ammonium moieties ( $R_4N^+$ ) and doped with ferric oxide nanoparticles (FeOnp)) achieve >95% phosphate removal from synthetic and municipal wastewater with competing anions (e.g.,  $Cl^-$ ,  $SO_4^{2-}$ ,  $HCO_3^-$ ) even at dilute phosphate concentrations (0.26–10 mg P/L).<sup>12–14</sup> Chemical regeneration with commercial base (i.e., NaOH) and electrochemically produced base (i.e., mixture of NaOH and NaCl) recovered >95% of adsorbed phosphate from HAIX sites.<sup>9,13,15</sup> FeOnp dopants in HAIX accelerated column regeneration due to shortened intraparticle diffusion length compared to undoped (no FeOnp) strong base anion exchange (SBA) resins.<sup>14</sup> Using HAIX, recovered phosphate can be transformed into valuable products, such as hydroxyapatite ( $Ca_5(PO_4)_3(OH)$ ) when paired with calcium<sup>12</sup> or struvite ( $MgNH_4PO_4 \cdot 6H_2O$ ) when paired with ammonium and magnesium.<sup>16</sup>

Adsorption conditions (e.g., solution pH, competing anions, and aqueous phosphate speciation) influence the capacity and selectivity of adsorptive phosphate recovery. Solution pH controls the relative abundance of different phosphate species (**Figure S2**), which exhibit unique affinities towards functional groups in HAIX (for  $R_4N^+$  groups:  $PO_4^{3-} > HPO_4^{2-} >$

$H_2PO_4^- > OH^-$ ). Similarly, the charge on FeOnp (i.e.,  $FeOH_2^+$ ,  $FeOH$ , or  $FeO^-$ ) depends on solution pH (**Figure S3**) and influences the nature of bonds between anions and FeOnp sites.<sup>12,17,18</sup> At circumneutral pH, phosphate adsorption occurs via inner-sphere ligand complexation with  $FeOH$ , and phosphate selectivity is achieved by the rejection of competing anions (e.g.,  $Cl^-$ ,  $SO_4^{2-}$ ,  $HCO_3^-$ ) that only form outer-sphere (electrostatic) complexes.<sup>13</sup> To enhance phosphate recovery and integrate HAIX into wastewater treatment, it is essential to optimize adsorption conditions. Dynamic adsorption modeling and process optimization require an understanding of the mechanisms underlying phosphate affinity in HAIX, specifically (1) where and how phosphate binds in HAIX resins and (2) how wastewater pH and competing ions (including organic matter) affect phosphate adsorption.

To date, mechanistic insights into HAIX phosphate selectivity have been limited to aqueous characterization (e.g., ion chromatography, spectrophotometry) by monitoring dissolved anion concentrations under different conditions. This approach provides a foundational understanding of adsorption behavior but leaves gaps in knowledge regarding the molecular mechanisms that govern selectivity. Specifically, aqueous characterization cannot distinguish phosphate binding to FeOnp sites versus functional groups in the polymeric matrix, limiting understanding of intrinsic selectivity in complex solutions. Intrinsic selectivity is vital for deconvoluting contributions from adsorbents and solutions, which enables systematic modeling and comparison of various wastewater compositions. Furthermore, relying on bulk pH does not completely elucidate functional group speciation because interfacial ion concentrations and resultant pH can differ from bulk conditions.<sup>19,20</sup> Direct characterization of the adsorbent is necessary to resolve these limitations. However, solid-phase characterization of HAIX has been limited to determining the speciation and distribution of iron oxides in the polymeric matrix using conventional techniques, such as XRD (X-ray diffraction) and SEM-EDX (scanning electron microscopy with energy dispersive X-ray analysis). While SEM-EDX provides valuable insights into iron distribution, its limited field of view (typically up to several mm) restricts the ability to assess heterogeneity across different resin beads (diameters of 0.3 to 1.2 mm). Furthermore, XRD cannot detect amorphous iron phases or assess spatial distribution of iron phase within a resin bead, both of which are crucial for phosphate affinity in wastewater.

Synchrotron techniques (e.g., micro-X-ray fluorescence ( $\mu$ -XRF), micro-X-ray absorption near edge structure ( $\mu$ -XANES) spectroscopy, and X-ray radiography)<sup>21,22</sup> can extend the capabilities of conventional techniques and provide molecular-level insights of chemical composition and elemental speciation on adsorbent surfaces. For example,  $\mu$ -XANES can reveal the oxidation state and local coordination environment of adsorbed phosphate, while  $\mu$ -XRF shows spatial distribution of key elements (i.e., phosphorus, chloride, and sulfur species) within resin structure, highlighting competitive adsorption or fouling

effects.<sup>10</sup> Furthermore, the relatively large field of view up to 25 mm) and microfocused beam ( $\sim 5 \times 5 \mu\text{m}$ ) allows for high-resolution imaging, and thus the simultaneous examination of multiple beads, that offers a more representative analysis. In comparison, SEM-EDX studies typically focus on a single bead, making them less representative of the overall sample. Furthermore, SEM is surface-sensitive, whereas  $\mu\text{-XRF}$  penetrates several micrometers, making it ideal for elemental mapping. Finally, radiography with tunable incident X-ray energy can provide visualization of FeOnp distribution and speciation within the adsorbent, helping to further reveal how iron phase and location can be leveraged to enhance phosphate adsorption in HAIX design. Together, these sensitive, spatially resolved X-ray techniques explain the distribution and speciation of iron in the adsorbent, the phosphate adsorbate, and competing ions (notably chloride and sulfate), providing a holistic description of phosphate selection mechanisms.

This study aims to elucidate phosphate adsorption mechanisms (distribution and speciation) in HAIX resins by combining aqueous-phase analysis and solid-phase, synchrotron-based X-ray characterization, applied to both simulated and real wastewater systems. To understand how material properties influence phosphate distribution and speciation, we collected comprehensive information on iron speciation in SBA- and WBA-HAIX resins with radiography and X-ray absorption spectroscopy (section 3.1). We complemented aqueous-phase analysis (of adsorption solution) with direct solid-phase measurements (of adsorbate, via  $\mu\text{-XRF}$  and  $\mu\text{-XANES}$ ) to determine phosphate distribution and speciation on HAIX post-adsorption (sections 3.2 – 3.4). Integrating synchrotron techniques with established aqueous characterization illuminated where and how phosphate binds in the resins. We used this integrated approach to evaluate the effects of several parameters (adsorbent dose, phosphate concentration, and presence of competing anions and organic matter) on phosphate adsorption and selectivity (section 3.5). Ultimately, our results advance understanding of molecular-scale adsorption interactions and elemental speciation within HAIX, and the findings can enable tailored adsorbent design and application for phosphate recovery.

## Materials and Methods

### 2.1 Aqueous Chemical Analysis

Anion concentrations ( $\text{Cl}^-$ ,  $\text{NO}_3^-$ ,  $\text{SO}_4^{2-}$ , and  $\text{PO}_4^{3-}$ ) before and after adsorption experiments were measured via anion chromatography (ion chromatography abbreviated IC, 4.5 mM sodium carbonate and 0.8 mM sodium bicarbonate eluent, suppressed, 1.0 mL/min, AS23-4  $\mu\text{m}$  column at 30 °C) on a Dionex ICS-6000 system (ThermoFisher Scientific, Waltham, MA). Total organic carbon concentration was measured on a Shimadzu TOC-L (Shimadzu Scientific Instruments, Inc., Columbia, MD). Aqueous iron concentrations were measured via ICP-OES (ICAP 6300 Duo View Spectrometer, Thermo-Fisher Scientific, Waltham, MA).

### 2.2 Preparation and Characterization of SBA and WBA HAIX Resins

We used two macroporous anion exchange adsorbents in this study: (1) a commercial strong-base hybrid anion exchanger (SBA-HAIX, FerriXA33E, Purolite, King of Prussia, PA) with a  $\text{R}_4\text{N}^+$  functional group and (2) a custom-functionalized HAIX (WBA-HAIX) resin from a commercial weak base anion exchange resin (HPR 9600, Amberlite, Wilmington, DE) with a tertiary amine functional group ( $\text{R}_3\text{N}$ ) (**Figure S4**).

WBA-HAIX functionalization with FeOnp was performed from a commercial WBA resin, according to a previously reported protocol<sup>23</sup> (full procedure in **Method S1** and schematic in **Figure S5**). We observed sulfate desorption from SBA-HAIX while rinsing the resins with water, likely from  $\text{FeSO}_4$  used during functionalization.<sup>12</sup> Thus, when preparing WBA-HAIX, we functionalized with  $\text{FeCl}_3$  as an alternative precursor that could avoid sulfate desorption. Photographs of the resins before adsorption are in **Figure S6**. We used scanning electron microscopy (SEM, FEI Magellan 400 XHR Scanning Electron Microscope, ThermoFisher Scientific, Waltham, MA) to obtain magnified images of the resins (with a 5.0 kV accelerating voltage and 50  $\mu\text{A}$  emission current). SEM images of the resins before adsorption are in **Figure S7**.

For simplicity and to focus on the key distinctions between resin types, we shorten SBA-HAIX to “SBA” and WBA-HAIX to “WBA” throughout the text. When referring to parent resins without FeOnp (i.e., only ammonium or amine sites), we state “without FeOnp”.

### 2.3 Batch Adsorption Experiments

To understand the effects of competing anions and organic matter on phosphate selectivity, we used five adsorption solutions of increasing complexity (full composition in **Table S1**). The solutions were (1) a pure 1 mM phosphate solution, (2) an equimolar solution of 0.5 mM phosphate and 0.5 mM sulfate (for equivalent conductivity to 1 mM phosphate), (3) a synthetic wastewater solution (SWW) modeled after a municipal wastewater influent with approximately 0.1 mM phosphate, (4) a synthetic wastewater solution with simulated organic matter (SWW + OM) with approximately 0.1 mM phosphate and 0.36 mM sodium acetate (a surrogate for organic species present in real wastewater), and (5) real wastewater effluent treated using anaerobic membrane bioreactor (RWW, Silicon Valley Clean Water, Redwood City, CA, composition in **Table S1**). In addition to these five solutions, we developed adsorption isotherms by preparing solutions containing 0.05 mM to 50 mM phosphate and 0.5 mM to 100 mM chloride. All adsorption solutions besides the real wastewater were prepared with nanopure water (MQ = Milli-Q, nanopure water with resistivity 18.2  $\text{m}\Omega\cdot\text{cm}$  at 25 °C, Millipore Milli-Q System, Millipore Corporation, Billerica, MA) and reagent-grade chemicals purchased from Sigma-Aldrich (St. Louis, MO). Because the resin dose (i.e., grams of resin per volume of solution) affects the overall

phosphate removal, we conducted experiments at 0.9 g/L and 2.0 g/L. Sample pH was measured with a pH meter (FP20, Mettler Toledo, Columbus, OH).

Resin performance was evaluated using three metrics: adsorption density, removal efficiency, and intrinsic phosphate selectivity against competing anions. Equation 1 defines the adsorption density  $q_f$  (mg of adsorbate/g adsorbent) for each adsorbate ( $A = \text{Cl}^-$ ,  $\text{SO}_4^{2-}$ , or  $\text{PO}_4^{3-}$ ).  $C_{0,A}$  and  $C_{f,A}$  are initial and final adsorbate concentration (mg/L), respectively, at equilibrium (adsorption measured after 24 hours),  $V_L$  is the solution volume (L), and  $M$  is the mass of resin (mg).

$$q_f = \frac{V_L(C_{0,A} - C_{f,A})}{M} \quad (1)$$

The removal efficiency for each adsorbate is the amount of adsorbate removed normalized by the adsorbate initially in solution (Equation 2):

$$\text{removal efficiency} = \left( \frac{C_{0,A} - C_{f,A}}{C_{0,A}} \right) * 100 \quad (2)$$

To account for differences in the initial concentrations of the adsorbates, we calculated the intrinsic selectivity ( $\alpha$ ) of phosphate ( $C_{0,P}$  and  $C_{f,P}$ ) against competing anions ( $C_{0,A}$  and  $C_{f,A}$ ) in solution using Equation 3:

$$\alpha_{P/X} = \frac{(C_{0,P} - C_{f,P})}{C_{0,P}} * \frac{C_{0,A}}{(C_{0,A} - C_{f,A})} \quad (3)$$

## 2.4 Column Adsorption Experiments

We conducted column experiments to understand the kinetic uptake of anions during adsorption and desorption during regeneration. Approximately 4.25 g of dry HAIX were packed into a column (35 mL volume, 1.5 cm inner diameter, 20 cm length) and 20 mM phosphate solution was pumped at 1 mL/min (Masterflex C/L, Vernon Hills, IL). For phosphate desorption, a 0.1 M NaOH regenerant solution was pumped at 1 mL/min. Effluent samples from adsorption and desorption experiments were collected every 5 - 15 minutes and measured on IC.

## 2.5 Micro-XRF and Micro-XANES for Anion Distribution and Phosphate Speciation

We employed several X-ray techniques, including  $\mu$ -XRF combined with  $\mu$ -XANES, radiography, and bulk X-ray absorption spectroscopy to characterize adsorbent surfaces before and after adsorption. This multiplex approach provided comprehensive insights into adsorbate binding mechanisms and adsorbent performance. Each technique offers unique advantages, such as differences in element mapping capabilities, spot size, and field of view (**Table S2**).  $\mu$ -XRF was combined with  $\mu$ -XANES to determine the relative distribution of phosphate and competing ions in adsorbent beads. To prepare samples for  $\mu$ -XRF and  $\mu$ -XANES analysis, unamended and post-adsorption resin beads (~50 mg) were dried at room temperature and thin-

sectioned (~100-200  $\mu\text{m}$ ) using a thin-sectioner (PetroThin Thin Sectioning System, Buehler, Lake Bluff, IL). Sectioning was performed to avoid self-absorption due to high phosphate concentrations in the samples. Prior to sectioning, resin samples were embedded in epoxy (Epotek 301) and glued to a 3 inch  $\times$  1 inch quartz slide.

Two-dimensional  $\mu$ -XRF maps of phosphorus (P), chloride (Cl), and sulfur (S) were acquired at SSRL beamline 14-3b. The measurements were conducted using a double Si (111) crystal monochromator at an incident X-ray energy of 4150 eV, with a spatial resolution of 5  $\mu\text{m}$  over a 2  $\times$  2 mm section of a resin-embedded sample. Fluorescence signals were detected using a seven-element Vortex Si-drift detector. To minimize X-ray attenuation in air, all samples were analyzed in a helium-purged chamber.

We analyzed  $\mu$ -XRF images with Sam's Microprobe Analysis Toolkit (SMAK 2.0).<sup>24,24</sup> MCA (Multi-Channel Analyzer) data, which consists of raw spectral information collected from the XRF detector for each image pixel, was fitted to extract elemental composition. These counts were then converted to surface concentrations ( $\mu\text{g}/\text{cm}^2$ ) using calibration with reference foils of known concentrations: GaP (101.1  $\mu\text{g}/\text{cm}^2$ ), KCl (98.8  $\mu\text{g}/\text{cm}^2$ ), and CuS (95.9  $\mu\text{g}/\text{cm}^2$ ).

To enable robust comparison between aqueous-phase and solid-phase results, elemental concentrations ( $\mu\text{g}/\text{cm}^2$ ) were converted to adsorption densities (mg/g). Resin beads were first differentiated from the epoxy background using particle statistics in SMAK, which identifies pixels corresponding to particles within an image and provides elemental composition data (in  $\mu\text{g}/\text{cm}^2$ ). The X-ray penetration depth into the sectioned resin surface was estimated using Hephaestus (a tool within the Demeter package), assuming the composition of HAIX in terms of FeOnp versus amine/ammonium sites. For SBA, we assumed that 40% of the total adsorption sites were FeOnps, and 60% were quaternary ammonium sites. For WBA, approximately 20% of the sites were assumed to be FeOnp, and 80% were tertiary amines. These assumptions were validated through a sensitivity analysis that minimized the residual sum of squares between aqueous- and solid-phase estimations (**Figure S8**). Finally, elemental concentrations obtained from SMAK particle statistics were converted to mg/g by dividing by the penetration depth and the dry density of the resins (0.7  $\text{g}/\text{cm}^3$  for both SBA and WBA). Dry density was used because the resin was dried for ~24 hours before preparing samples for solid-state measurements.

To understand the chemical speciation of adsorbed phosphate on HAIX, we complemented  $\mu$ -XRF with  $\mu$ -XANES. Phosphorus K-edge XANES spectra (at energy ~2150 eV) were obtained at multiple spatially resolved spots on the resin that allowed us to distinguish phosphate binding interactions, specifically differentiating between its association with the polymeric matrix and its interaction with the FeOnp in HAIX. In addition to collecting XANES on the resins, we collected spectra for various standards including phosphate adsorbed to (1) strong base anion exchange resin without FeOnp (IRA 400 chloride form, Amberlite, Wilmington, DE), (2) weak base anion exchange



resin without FeOnp (HPR 9600), (3) goethite, and (4) ferrihydrite. Combined  $\mu$ -XRF and  $\mu$ -XANES enhances understanding of the speciation, distribution, and concentration of phosphorus in HAIX under different wastewater compositions.

Phosphorus K-edge XANES spectra were processed in ATHENA<sup>25</sup> using background subtraction, normalization, and averaging. A linear pre-edge function (ranging from 26.4 to 10 eV below the edge) was fitted and subtracted for background removal and then normalized by fitting a linear function to the post-edge region (6.3–86.4 eV above  $E_0$ ). Additionally, we employed linear combination fitting to quantify phosphate adsorption onto FeOnp sites and polymeric sites (quaternary ammonium for SBA and tertiary amines for WBA). For FeOnp sites, phosphate adsorption was assessed using both goethite- and ferrihydrite-adsorbed phosphate as standards, and their respective contributions were summed to determine total phosphate adsorption onto FeOnp sites.

## 2.6 Bulk X-ray absorption spectroscopy and Radiography for Iron Distribution and Speciation

To examine iron speciation, X-ray absorption spectroscopy was conducted on virgin SBA and WBA at SSRL beamline 4-3 (spectra in **Figure S9a**). The beamline features a Si (111) double-crystal monochromator ( $\phi = 90^\circ$  orientation) and a Si mirror for harmonic rejection. For sample preparation, the beads were finely ground using a mortar and pestle, and approximately 2 mg of resin were mixed with  $\sim 20$  mg of boron nitride to minimize X-ray attenuation during iron spectral acquisition in transmission mode.

In addition to the sample spectra, we also collected spectra from various iron standards to quantitatively assess the iron species present in SBA and WBA (**Table S3**). Similar to the sample preparation, the standards—siderite ( $\alpha$ -FeCO<sub>3</sub>), Fe(II) sulfate ( $\alpha$ -FeSO<sub>4</sub>), ferrihydrite ( $\alpha$ -(Fe<sup>3+</sup>)<sub>2</sub>O<sub>3</sub>·0.5H<sub>2</sub>O), hematite ((Fe<sup>3+</sup>)<sub>2</sub>O<sub>3</sub>), and goethite ( $\alpha$ -FeO(OH))—were prepared by grinding  $\sim 1$ –2 mg of each iron mineral with 20 mg of boron nitride using a mortar and pestle (spectra of standards shown in **Figure S9b**).

To investigate iron speciation within SBA and WBA resin beads, we collected radiographs of iron species in transmission mode at SSRL beamline 6-2b at different energies around the Fe absorption edge. The beamline has a Si (111) double-crystal monochromator ( $\phi = 0^\circ$  orientation), harmonic rejecting mirror, and vertical focusing mirror. Radiography while scanning the incident X-ray energy across the iron K-edge enables spatially resolved iron distribution mapping over a larger area compared to other analytical techniques, such as energy-dispersive X-ray analysis (EDX), making it particularly suitable for analyzing the 300–1200  $\mu$ m diameter SBA-HAIX and WBA-HAIX resin beads in this study.

For radiography sample preparation, resin beads were embedded in epoxy and sectioned to a thickness of  $\sim 100$

$\mu$ m. These thin sections minimized X-ray attenuation from high iron concentrations, ensuring accurate iron mapping. Iron XANES radiographs were collected for both SBA and WBA resins with the following parameters: Region 1 (7050–7100 eV) at a step size of 5 eV; Region 2 (7101–7161 eV) at a step size of 1 eV; Region 3 (7162–7203 eV) at a step size of 2 eV; and Region 4 (7204–7424 eV) at a step size of 5 eV. These parameters facilitated a smooth Fe XANES spectra for each radiograph pixel, particularly in the pre-edge region. For each sample, both sample and reference images were collected to convert from transmission to absorption through the Beer-Lambert law with a nonuniform beam profile. The collected data was analyzed using TXM Wizard.<sup>26</sup> After reference correction, the images were processed in XANES Wizard within TXM Wizard. To assess iron speciation variation within the resin beads, each sample was segmented into two distinct regions: core and periphery (details in **Figure 1** and **Figure S10**). XANES spectra from each region were extracted and saved for further processing. Both bulk and imaging XANES spectra were processed (background subtracted and normalized) in the ATHENA suite of Demeter package. Linear combination fitting was then used to determine the abundance of iron species.

## Results and Discussion

### 3.1 Iron Distribution and Speciation in Unamended Resins

We used synchrotron-based X-ray techniques to analyze the distribution and speciation of iron (as FeOnp) in strong base (SBA) and weak base (WBA) resins prior to adsorption (**Figure 1**). Iron distribution on resins has previously been examined using scanning electron microscopy energy-dispersive X-ray spectroscopy (SEM-EDX),<sup>14,23</sup> which has high spatial resolution but high minimum detection limits and is prone to artifacts. Similarly, iron speciation has been previously analyzed using XRD and Mössbauer spectroscopy,<sup>27</sup> which have no spatial resolution because they are bulk measurements. Determining the iron phases is critical because it will impact the phosphate binding behavior and stability of the iron oxide nanoparticles.<sup>28</sup> Understanding phosphate binding to various iron phases is essential for optimizing the amount and type of iron phase in future adsorbent design. Additionally, iron oxide nanoparticle stability is critical for wastewater applications to minimize environmental burden from iron desorption and extend lifetime for cost reduction. Compared to existing methods (SEM-EDX, XRD, Mössbauer), synchrotron-based X-ray techniques, such as  $\mu$ -XRF and radiography, provide high spatial resolution, a larger field of view (and therefore more representative as multiple beads can be analyzed), and lower detection limits. Synchrotron-based methods also enable quantitative analysis of iron speciation (comparison of methods in **Table S2**).

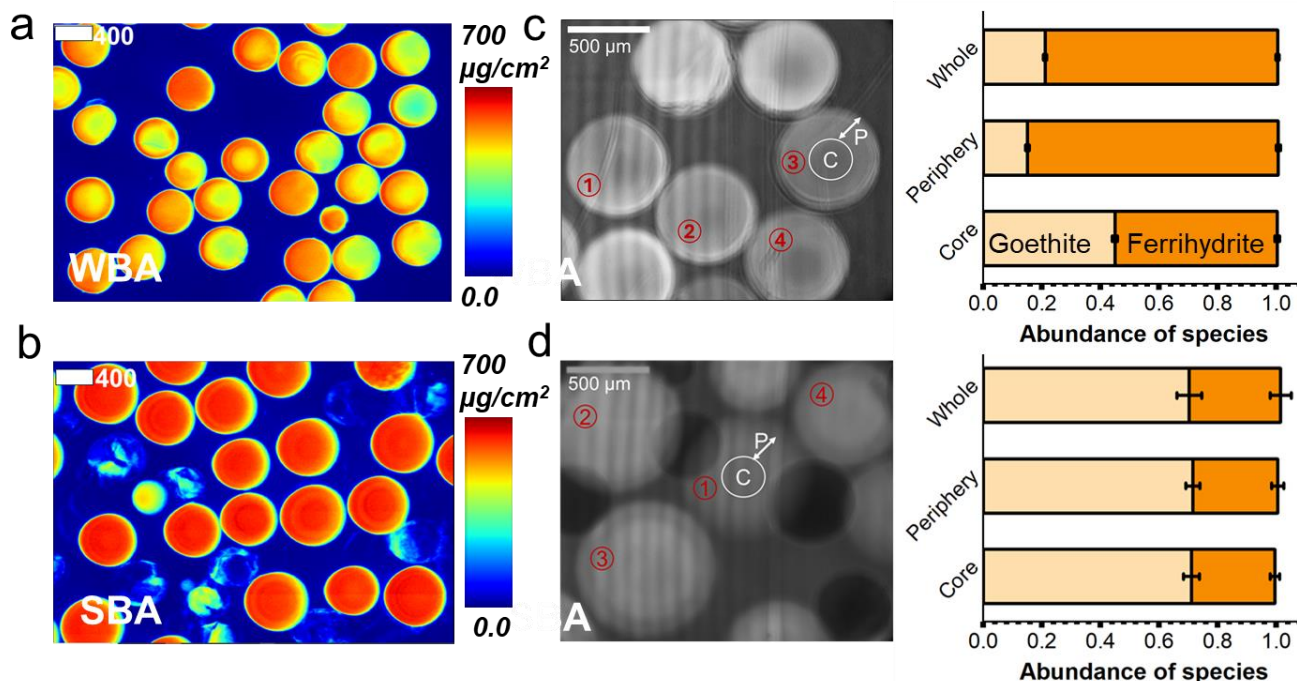


**Figure 1. Iron distribution and speciation in SBA and WBA.** (a) and (b) Iron distribution in SBA and WBA resins, measured via XRF mapping at BL 2-3. (c, d) radiographs defining resin core (C) and periphery (P) locations and abundance of iron species for (c) WBA and (d) SBA. Abundance of iron species was obtained by averaging the Fe species abundances in the four resins analyzed. Error bars are from measurements of four different beads and represent one standard deviation above or below the average.

To quantify iron speciation, we measured bulk X-ray absorption spectra of both resins and various iron mineral standards (Figure S9). Linear combination fitting (LCF) was used to fit the XANES spectra to corresponding iron phases, revealing a mixture of goethite and ferrihydrite in both SBA and WBA resins (Figure S10-11, Table S4). Specifically, bulk WBA exhibited more ferrihydrite (65%) than goethite (35%), while bulk SBA was predominantly composed of goethite (80%) with a minor ferrihydrite fraction (20%).

Previously, FeOnp within resins have been broadly characterized as hydrated or hydrous ferric oxide, with limited identification of specific iron phases.<sup>27</sup> Belloni et al. performed Mössbauer spectroscopy to elucidate speciation of several anion exchange resin types and concluded 100% goethite for a commercial SBA (LayneRT).<sup>27</sup> In their SBA resin prepared with FeCl<sub>3</sub> (same iron precursor as our WBA sample but different backbone), they observed 60 – 80% goethite and attributed the other 20 – 40% to either ferrihydrite or superparamagnetic goethite.<sup>27</sup> Their overall conclusion of more goethite in the commercial samples prepared with FeSO<sub>4</sub> compared to samples doped with FeCl<sub>3</sub> aligns with our findings of more goethite in SBA than WBA. The difference in quantitative amounts could be due to difference in supplier or the lower spatial resolution of Mössbauer spectroscopy compared to  $\mu$ -XANES (Table S2).

In addition to bulk spectroscopy, we utilized XANES radiography, which provides an Fe spectrum for every pixel of the imaged area. We examined Fe speciation in pixels

from the core of the resin beads and from the periphery to evaluate whether different diffusion rates of the iron precursors into the resins could result in different speciation. LCF revealed that the WBA resin was more ferrihydrite-rich in both the averaged whole (79%) and periphery (86%) compared to the core (55%) (Figure 1c). In contrast, the SBA resin exhibited a more homogeneous distribution of goethite across the averaged whole, periphery, and core (70%, 72%, and 71%, respectively) (Figure 1d). The difference in iron phases is likely due to a difference in iron precursors (i.e., commercial SBA is prepared with FeSO<sub>4</sub>, and WBA was prepared with FeCl<sub>3</sub>). The iron phase could also be related to reaction time, because ferrihydrite is metastable and gradually converts to more stable phases (goethite, hematite, lepidocrocite) over time. Thus, extending the reaction time during functionalization may convert ferrihydrite to goethite.<sup>29,29</sup>

Using  $\mu$ -XRF, we observed a uniform, homogeneous distribution of FeOnp in SBA (Figure 1b). Note that one resin bead in the field of view as an outlier that exhibited lower iron concentration in the core than periphery. However, in WBA, we observed higher FeOnp distribution on the periphery of the resins (Figure 1a). We attribute the difference in FeOnp distribution between the SBA and WBA types to differences in porosity and iron precursors. Specifically, a lower porosity in WBA likely hindered diffusion of iron during functionalization, leading to a higher concentration on the resin periphery. SEM imaging qualitatively compared resin porosity and revealed that the



external surface of SBA was more porous than WBA based on the number and size of surface pores (**Figure S7**). To ensure that our functionalization process was not responsible for the limited porosity, we also imaged the unmodified resin (without FeOnp) and observed the same low external porosity (**Figure S7c**). WBA resins have less crosslinking that leads to lower permanent porosity in the polymeric structure.<sup>17,23</sup> Another possible explanation for the non-uniform FeOnp distribution in WBA is the use of Fe(III) as a precursor, in contrast to Fe(II) in SBA. Fe(III) more readily precipitates as iron hydroxides, leading to localized deposition, whereas Fe(II) remains more soluble under acidic and neutral pH conditions, allowing for penetration into the core and more uniform distribution.<sup>30</sup> The influence of porosity and iron impregnation on FeOnp distributions motivates further investigation into rational adsorbent design to maximize phosphate adsorption and iron stability.

### 3.2 Evaluating Phosphate Recovery from Wastewater Solutions with Synchrotron Techniques

Synchrotron techniques for solid-phase adsorbent characterization enable comprehensive understanding of phosphate adsorption distribution and speciation. We employed  $\mu$ -XRF to analyze the resins before (**Figure S12**)

and after adsorption (**Figure 2**), offering complementary insights to conventional aqueous-phase adsorption analysis. Notably, while aqueous analysis indirectly estimates adsorption density using ion concentrations in solution before and after adsorption, solid-phase X-ray techniques enable direct characterization of adsorbates on the resin surface. The ability to visualize adsorbate distribution on adsorbent sites enables understanding of the selective phosphate adsorption mechanism. We tested and imaged the resins in a series of wastewaters (**Table S1**) of increasing complexity to evaluate the impact of competing ions on phosphate adsorption (**Figure 2**).  $\mu$ -XRF images mapped the distribution of phosphate (as phosphorus, **Figure 2a,c**), sulfate (as sulfur, **Figure 2b,d**), and chloride (Cl, **Figure S13-15**) on SBA and WBA resins after adsorption.

As expected, the phosphorus concentration observed in  $\mu$ -XRF mapping varied directly with the phosphate concentration in the initial wastewater solution. The  $\mu$ -XRF map of both resins after adsorption from a 1 mM phosphate solution showed higher phosphorus concentrations than those after adsorption from a 0.5 mM phosphate solution. For example, the SBA resin had a mostly homogenous  $>15 \mu\text{g}/\text{cm}^2$  ( $35\text{--}45 \mu\text{g}/\text{cm}^2$ ) phosphate concentration after

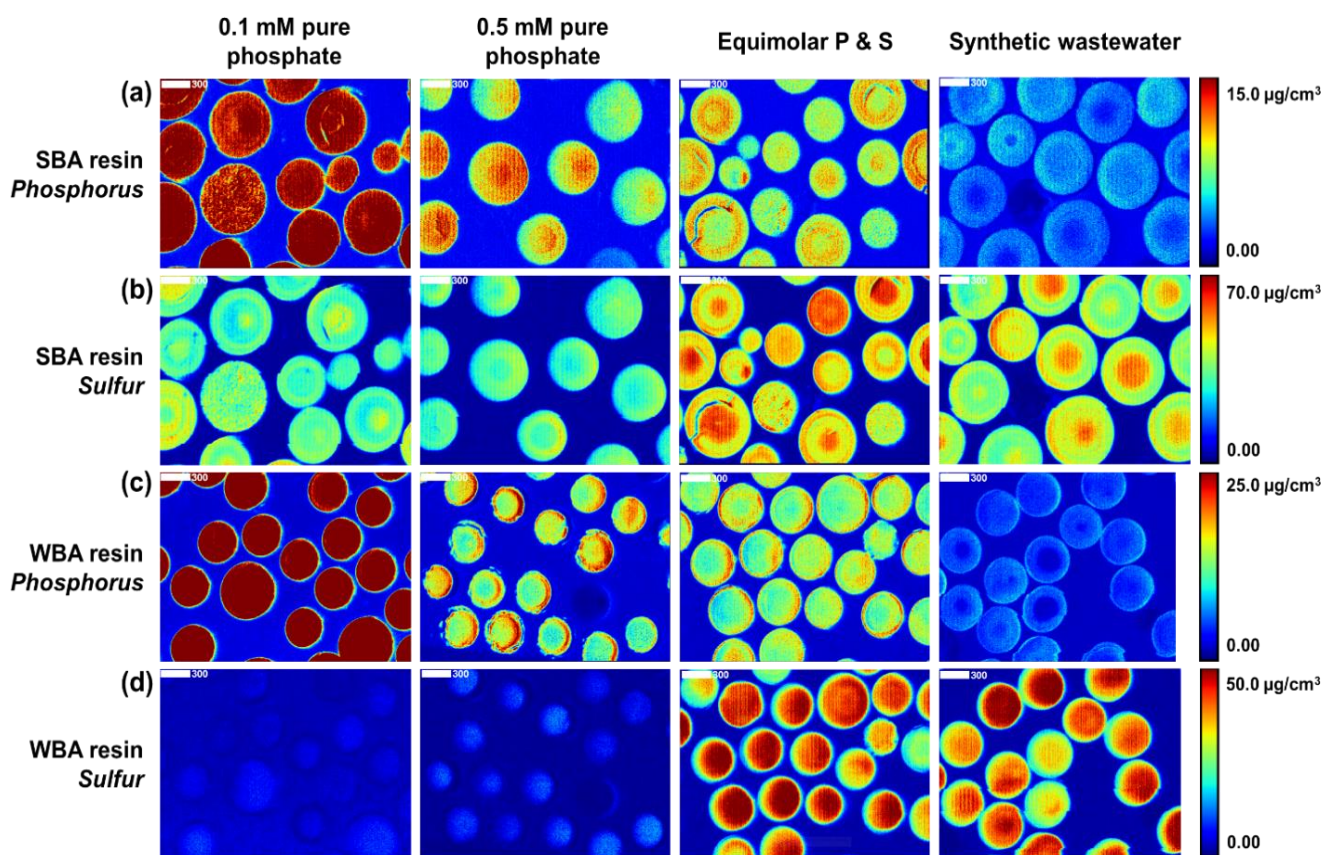


**Figure 2. Phosphorus and sulfur distribution on resins after adsorption from synthetic wastewater solutions of increasing complexity, measured via  $\mu$ -XRF. (a,b)** Phosphorus and sulfur distribution on strong base resin (SBA), respectively. **(c,d)** Phosphorus and sulfur distribution weak base resin (WBA) after phosphate adsorption. Pure phosphate (1 mM and 0.5 mM phosphate), equimolar phosphate & sulfate (0.5 mM phosphate and 0.5 mM sulfate), and synthetic wastewater solutions are shown here; synthetic wastewater with organic matter and real wastewater are in Figure 6.

adsorption from the 1 mM phosphate solution, in contrast to the 5 - 15  $\mu\text{g}/\text{cm}^2$  concentration observed after adsorption from the 0.5 mM solution. Similarly, approximately 25 - 50% lower phosphate concentrations were observed for equimolar P/S (0.5 mM phosphate) and synthetic wastewater (0.17 mM phosphate) compared to the 1 mM phosphate solution.

The phosphate concentration of the adsorption solution also influences intraparticle diffusion and consequently phosphate distribution. Intraparticle diffusion refers to internal phosphate diffusion to the adsorption sites in the resin, as opposed to external phosphate diffusion from the bulk solution to the resin surface. At low phosphate concentration (0.1 - 0.5 mM), adsorption was primarily on the resin periphery (**Figure 2a**, equimolar P/S and synthetic WW). At higher initial phosphate concentrations (1 mM), adsorption was also observed in the core of the resin (**Figure 2a**, pure phosphate).

The  $\mu$ -XRF maps also yielded valuable insights into differences between SBA and WBA resins in terms of the distribution of phosphate and sulfate. After adsorption from a pure phosphate solution, the phosphate distribution within SBA resin was homogenous and consistent with the iron distribution in **Figure 1b**. In contrast, WBA exhibited high concentrations of phosphorus on the outer resin periphery compared to sulfur. This distribution was also consistent with the concentrated peripheral iron observed in **Figure S1a**, which was attributed to lower porosity of the WBA resin. In both SBA and WBA, the overlapping phosphate and iron distributions indicates selective adsorption of phosphorus to the FeOnp sites. If phosphate adsorption primarily occurred at the ammonium functional groups, we would expect a more homogenous phosphate distribution across the WBA resin. Instead, the phosphate distribution closely aligned with the spatial iron distribution within the resin. The alignment between phosphorus concentration and iron distribution is supported by previous work in which resins with more surface iron exhibited more surface adsorbed phosphate.<sup>14</sup> We note that intra-batch variation can lead to a few resin beads with more surface-distributed FeOnp in SBA as well, such as the lone heterogeneous resin bead in **Figure 1b** or the bead with more surface FeOnp in images by Dong et al.<sup>14</sup>

Unexpectedly, we observed a high concentration of sulfur in the fresh, pre-adsorption SBA resin (**Figure S12, S15**) and the resin after pure phosphate adsorption (**Figure 2a, S15**) - both of which should contain no sulfate. We hypothesized this sulfate resulted from contamination during the manufacturing process,<sup>13,31</sup> which was supported by a lack of sulfate in the WBA samples prepared with a  $\text{FeCl}_3$  precursor instead of  $\text{FeSO}_4$ . Similarly, a high background concentration of Cl was observed in virgin WBA beads (**Figure S12, S14-15**) and even in pure phosphate solutions, primarily due to residual Cl from  $\text{FeCl}_3$  used during the functionalization process. The elevated chloride concentration at the periphery of virgin beads in both SBA and WBA is attributed to the epoxy used during sectioning, which complicates background removal (**Figure S12**). The impact of these pre-existing contaminants and counter ions

on the phosphate adsorption performance is discussed more in section 3.5.1.

### 3.3 Phosphorus Speciation

To expand upon the insights on phosphate distribution from section 3.2, we examined phosphorus speciation, specifically which sites phosphate is binding to, using phosphorus K-edge  $\mu$ -XANES (**Figure 3, S16-S19**). The pre-edge feature indicates selective binding of phosphate to iron sites<sup>32</sup>, supported by the  $\mu$ -XRF analysis (section 3.2). We quantified the amount of phosphate that binds to FeOnp sites versus quaternary ammonium sites by comparing standards for phosphate binding to only quaternary ammonium sites and to only FeOnp sites (**Figure S20**). We fit  $\mu$ -XANES spectra to both goethite and ferrihydrite standards because the pre-edge feature intensity is a function of denticity as well as the iron phase. Bidentate phosphate generally corresponds to higher pre-edge feature intensities, regardless of phase, making it challenging to fit to specific iron phases.<sup>32</sup> However, because there is no pre-edge feature in phosphate bound to resins without FeOnp (**Figure S20**), we can differentiate between phosphate bound to ammonium sites (no pre-edge feature) and phosphate bound to FeOnp sites (pre-edge feature). Note that this analysis differs from the analysis presented in **Figure 1**. **Figure 1** refers to the total number of available FeOnp sites in the resin, and **Figure 3** refers to the amount of phosphate bound to these FeOnp sites. For both SBA and WBA, 1 mM pure P led to higher binding on quaternary ammonium and tertiary amines as compared to other conditions, likely due to phosphate penetrating further into the core and accessing more functional groups. Additionally, it is likely that 1 mM phosphate saturated FeOnp sites leading to adsorption on low affinity ammonium/amine sites. Directly comparing 0.5 mM pure P and 0.5 mM eq. P/S showed that sulfate lowers phosphate binding to FeOnp in the core due to competition for sites. In all solutions, phosphate binding to FeOnp sites was greater in WBA than in SBA, likely due to the higher ferrihydrite content in WBA, which provides more surface-active sites for adsorption compared to the goethite-rich SBA.

In SBA (**Figure 3e**), phosphate binding to iron was approximately the same in the periphery and core, which is supported by the homogenous distribution of phosphate in the  $\mu$ -XRF maps (**Figure 2**). More notable differences were observed between the periphery and core in WBA (**Figure 3f**), following the heterogeneous iron distribution (**Figure 2**). The alignment of phosphate and FeOnp distributions underscores the selective binding of phosphate to FeOnp sites.

To elucidate the effect of pH on phosphate binding, we evaluated phosphate adsorption density and removal in 1 mM phosphate solutions with pH 5, 7, and 9 (**Figure S21**, composition in **Table S5**). Both the phosphate and FeOnp speciation in solution will change as a function of pH (**Figures S2 and S3**). For phosphate, there is an interplay between  $\text{H}_2\text{PO}_4^-$  (dominant at lower pH) and  $\text{HPO}_4^{2-}$  (dominant at higher pH). The more negatively charged phosphate at higher pH favors attraction to the ammonium



groups. Thus, reducing the pH will reduce binding on ammonium sites. For iron, there is an interplay between  $\text{FeOH}_2^+$  (dominant at lower pH),  $\text{FeOH}$  (dominant at pH 7–9), and  $\text{FeO}^-$  (dominant at higher pH). The negatively charged ion groups will repel the negatively charged phosphate, and thus adsorption on iron sites decreases as the pH is increased.

In aqueous-phase analysis, phosphate adsorption density varied between 35–45 mg P/g resin across pH solutions for both SBA and WBA, and adsorption density generally decreased as the solution pH increased, as expected due to changing FeOnp speciation.<sup>14</sup> Similarly, phosphate removal efficiency decreased as the pH increased and was higher in SBA than WBA at all pH values. The decreasing phosphate uptake with increasing pH further supports phosphate binding to FeOnp. Increasing pH leads to reduced phosphate adsorption on FeOnp but little change on

ammonium sites, making elevated pH an effective strategy for site-selective regeneration.<sup>12,23</sup>

We complemented the aqueous phase analysis with solid-state characterization to determine any differences in phosphate binding location (core vs periphery) across adsorption solutions (**Figure S22**). In WBA, we observed the fraction of phosphate adsorbed to FeOnp decrease as the pH is increased to 9 (**Figure S23, S24**), again due to the changing iron speciation to  $\text{FeO}^-$ . The pH of the adsorption solution (pH 5 and 9) had little effect on the binding sites for SBA, although a stronger impact is expected at more extreme pH values. The insights gained into phosphate binding locations at different pH values are crucial for understanding the adsorption mechanism in a variety of wastewaters and regenerant solutions.

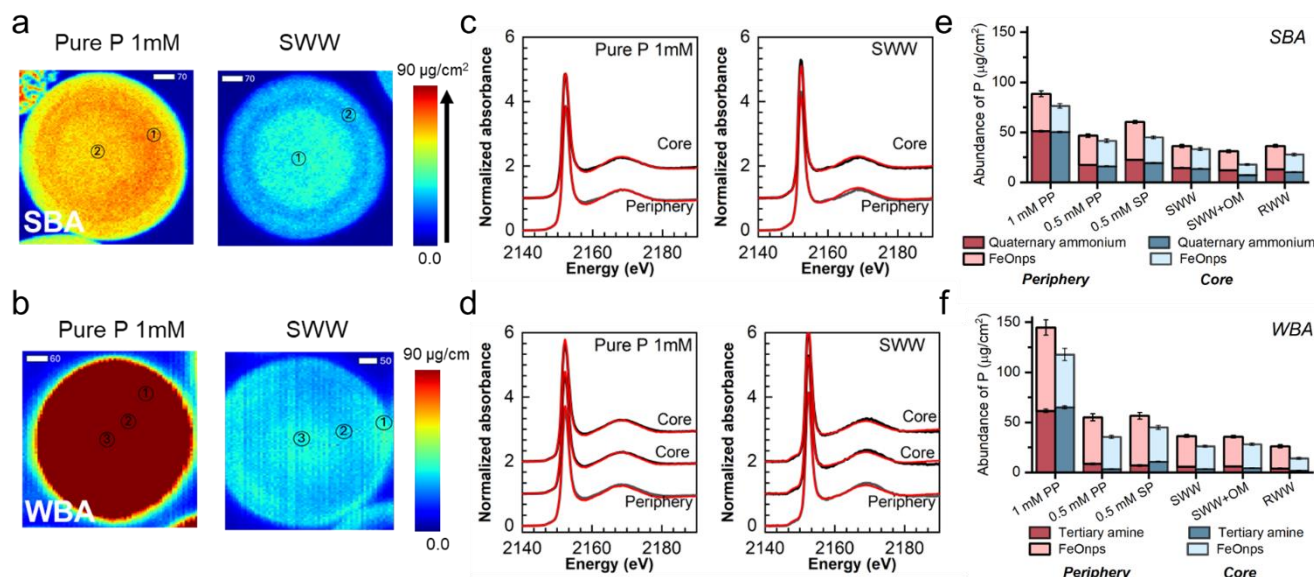


**Figure 3. Phosphorus speciation and distribution.** (a, b) XRF images of phosphorus on SBA and WBA resins after adsorption from 1 mM pure P solution and SWW; locations chosen for core, middle, and periphery measurements are marked, (c, d) XANES spectra measured at core, middle, and periphery locations marked in (a, b), (e, f) ratio of P bound to FeOnp sites vs. P bound to polymeric ammonium/amine sites.

### 3.4 Comparing Solid-Phase Characterization of Phosphate Recovery with Aqueous-Phase Characterization

To validate the high-resolution insights gained from synchrotron-based solid-phase analysis, we quantified adsorption densities from aqueous-phase batch analysis for both SBA and WBA (**Figure 4**). Using post-processing in SMAK 2.0 (full method is described in **Section 2.5**), we obtained the phosphate adsorption density values from XRF maps and compared them to the aqueous adsorption results (**Figure 4**). To the best of our knowledge, this study is the first to (1) quantify adsorption densities obtained via solid-phase, synchrotron-based characterization and (2) directly compare solid-phase and aqueous-phase adsorption methods. We used a residual sum of squares analysis to determine the ratio of FeOnp to ammonium sites that

resulted in the lowest error between aqueous and solid-state measurements across solutions (**Figure S8**).

Notably, the adsorption densities obtained via quantitative analysis of the XRF maps closely aligned with those measured using aqueous analysis (**Figure 4**), which validates solid-phase techniques for accurately quantifying adsorption. Out of the 10 resin-solution pairs tested, only the SBA pure phosphate conditions showed significant deviation between aqueous and solid-state measurements (p-value of 0.0285 for the two means with two-sample t-test). We attribute this difference between aqueous and solid-state measurements to the high concentration of phosphate in the resin that reduced the penetration depth of X-rays. This attenuation results in low fluorescence signal and hence lower phosphorus counts. Additionally, the

higher Fe concentration in SBA results in a reduced X-ray penetration depth (SBA: 21  $\mu\text{m}$ , WBA: 37  $\mu\text{m}$ ), which may have also contributed to this difference.

For simplicity, only the 2 g/L resin dose is shown in **Figure 4**. A comparison of adsorption density and removal efficiency between 0.9 g/L and 2 g/L resin doses is shown in **Figure S25**. Resin doses of 0.9 and 2 g/L were chosen for initial aqueous analysis to (1) achieve appreciable adsorption densities that could be observed via solid-state analysis and (2) avoid the saturating adsorption sites of the resins, as differentiating between site affinity in wastewaters is challenging if all of the sites are filled. Ultimately, the 2 g/L resin dose was prioritized over 0.9 g/L for synchrotron analysis because it enabled a greater phosphate removal efficiency that is more relevant to wastewater treatment applications.

As expected, increasing the resin dose from 0.9 to 2 g/L led to a decrease in phosphate uptake per g resin and increase

in removal efficiency across all solutions, except for one statistically significant outlier (WBA in equimolar solution of phosphate and sulfate with a p-value of 0.0141 after a two-sample t-test). In the 1 mM pure phosphate solution, WBA resins exhibited a higher phosphate adsorption density compared to SBA resins (**Figure 3a** vs. **Figure 3b**), likely due to the high ferrihydrite content that provides more surface-active sites for phosphate adsorption. Thus, both resin iron distribution and speciation influence the phosphate removal performance. Notably, with a higher resin dose (2 g/L), SBA and WBA removed phosphate from a variety of wastewaters with over 60% efficiency (**Figure S25**). In contrast to pure P solutions, SBA outperforms WBA in more complex solutions due to a higher number of FeOnp sites, which other ions cannot bind to via inner-sphere ligand complexation.<sup>14</sup>

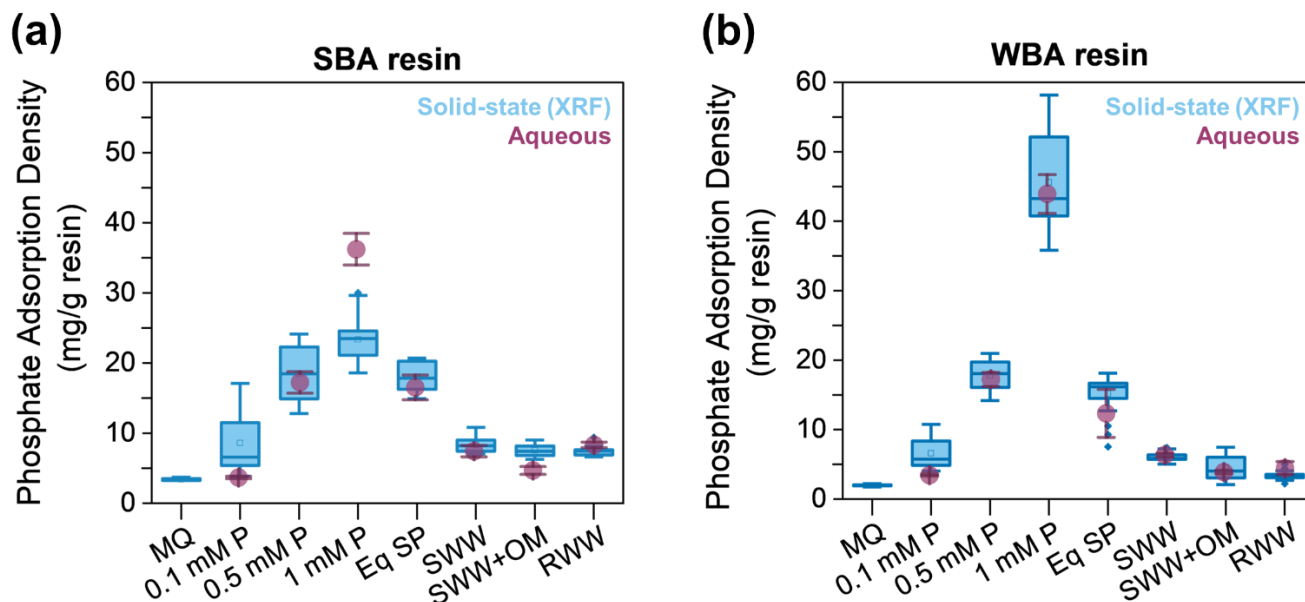


**Figure 4. Quantitative comparison of adsorption performance between aqueous and solid-phase (synchrotron) analysis at 2.0 g/L.** Phosphate adsorption density for **(a)** SBA resin and **(b)** WBA resin from a variety of solutions, including 1 mM pure phosphate (P), equimolar sulfate/phosphate (eq S/P), synthetic wastewater without (SWW) and with organic matter (SWW+OM), and real wastewater (RWW). MQ refers to resin soaked in MQ water for 24 hours. XRF maps used for quantification are in Figures 2, 6, and S11.

### 3.5 Competitive Counterion Adsorption on HAIX

#### 3.5.1 Effect of Inorganic Anions on Phosphate Adsorption

To determine the effect of competing ions in each solution, we compared phosphate adsorption density in wastewater to the pure phosphate solutions with equivalent concentrations (**Figure 4**). Specifically, the equimolar P/S solution can be compared to 0.5 mM pure P, and the SWWs can be compared to 0.1 mM pure P. For both SBA and WBA, there is no significant difference (p-value = 0.6 and 0.06, respectively) between the pure phosphate solution and solution with sulfate, suggesting that sulfate competition had minimal impact on phosphate adsorption. In contrast, there was a significant difference for both SBA and WBA between the pure phosphate solution and synthetic wastewater (p-value = 0.013 and < 0.00001, respectively), suggesting that the competing ions in the synthetic wastewater negatively impacted phosphate adsorption.

Pre-existing anions on the resins can also affect selectivity measurements. XRF images of virgin resins (pre-adsorption) show primarily sulfur in SBA (up to 100  $\mu\text{g}/\text{cm}^2$ ) and chloride in WBA (up to 200  $\mu\text{g}/\text{cm}^2$ ) (**Figure S12**). Both anions are residual from the iron doping procedure;  $\text{FeSO}_4$  and  $\text{FeCl}_3$  are used for SBA and WBA, respectively.<sup>13,23,31</sup> SBA also contains chloride (up to approximately 60  $\mu\text{g}/\text{cm}^2$ ), which is the counterion on the quaternary ammonium groups. A small amount of sulfur (up to 60  $\mu\text{g}/\text{cm}^2$ ) was observed in WBA. Sulfur has been observed previously in commercial anion exchange resins,<sup>27</sup> and it is likely residual from the synthesis procedure. The resin was not washed prior to the experiments, which may have contributed to the observed sulfur content. During batch and column experiments, the chloride and sulfate are released either through desorption or exchange during

phosphate adsorption, leading to an increased aqueous concentration of both species after phosphate adsorption (**Figure S26, S27**). In the HAIX systems studied, desorption refers to a non-phosphate ion leaving the resin because of its own activity gradient, whereas exchange refers to ion release due to adsorption of ions of higher affinity or abundance (**Figure S28**). We elucidated the leaving mechanism of each ion (i.e., desorption versus exchange with phosphate) by comparing their concentrations after adsorption in a phosphate solution versus nanopure MQ (**Figure S26**).

In SBA, chloride release was more prominent after phosphate adsorption than after soaking in MQ (**Figure S26a, left**), aligning with our understanding that chloride is the counterion on the ammonium groups and exchanges with phosphate. Sulfate is likely an impurity in SBA from the manufacturing process. We also observed higher release in the phosphate solution (**Figure S26b, left**), which could be due to sodium counterions facilitating charge balance in the phosphate solution. Additionally, sulfate may have replaced chloride on some of the ammonium groups and be exchanging with phosphate, leading to higher sulfate concentration in the phosphate solution than the MQ solution.

WBA was prepared with  $\text{FeCl}_3$  rather than  $\text{FeSO}_4$ , and consequently, high chloride release was observed (**Figure S26a, right**). Similar to sulfate release from SBA, the chloride release was higher in phosphate solution compared to the MQ solution (**Figure S26b, right**), likely due to the sodium counterions facilitating charge balance. We also observed small amounts of sulfate release from WBA in both MQ and 1mM PP. Similar to SBA, we attribute the sulfate to impurities from manufacturing.

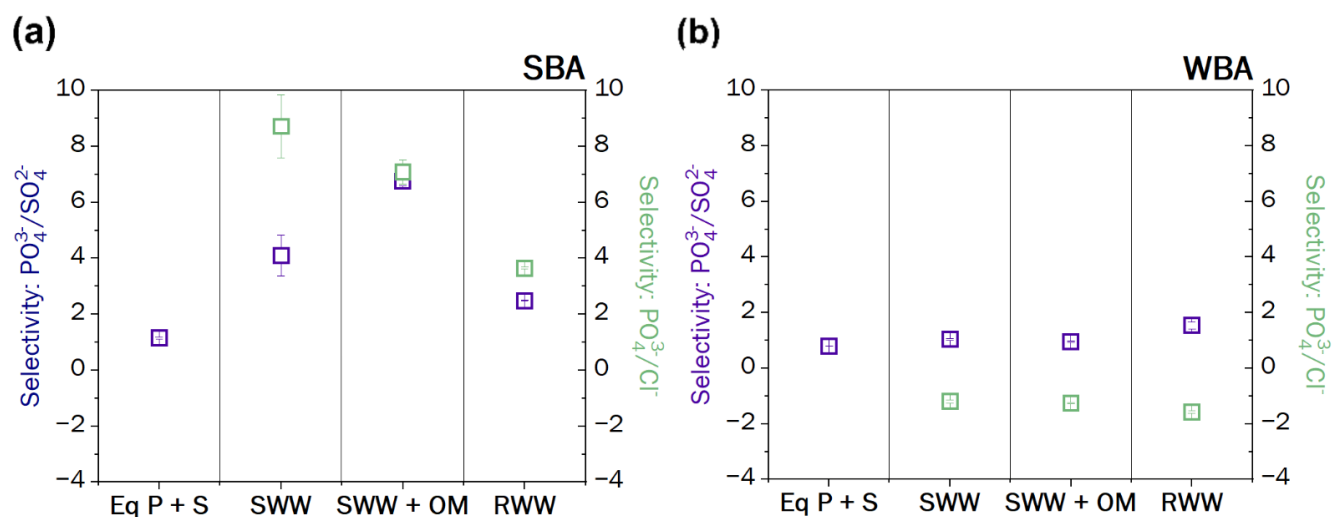


**Figure 5. Anion selectivity across adsorption solutions.** Phosphate selectivity against competing anions for (a) SBA resin and (b) WBA resin across various solutions of increasing complexity at 2.0 g/L. Eq P + S = equimolar phosphate/sulfate, SWW = synthetic wastewater, SWW + OM = synthetic wastewater with organic matter, RWW = real wastewater. Error bars not shown are smaller than symbols. Initial composition of each solution is in Table S1; briefly, sulfate is present in all solutions in Figure 5; chloride is present in all except for Eq P+S.



Despite ample investigation into HAIX for phosphate removal, existing literature primarily reports selectivity values relative to competing anions (e.g., sulfate, chloride, nitrate) without accounting for initial feed concentrations or elucidating the kinetic mechanisms that govern phosphate adsorption in multicomponent solutions. To elucidate the contribution of FeOnp to phosphate selectivity, we evaluated the intrinsic selectivity of phosphate against chloride and sulfate on each resin type across wastewater solutions (**Figure 5**). Because chloride and sulfate are desorbed or exchanged from the resin during adsorption, the reported selectivity values represent the overall net selectivity, accounting for both adsorption and desorption. Chloride desorption hindered the  $\text{PO}_4^{3-}/\text{Cl}^-$  selectivity in WBA across the chloride-containing solutions. Excess chloride in WBA from  $\text{FeCl}_3$  synthesis led to negative adsorption densities, contrasting with positive adsorption isotherm values measured after initial chloride removal with MQ (**Figure S27**).

At the 2.0 g/L resin dose, phosphate selectivity over sulfate increases with solution complexity, while selectivity over chloride gradually decreases across chloride-containing solutions (**Figure 5a**, no  $\text{Cl}^-$  in equimolar P + S solution). This decrease in  $\text{PO}_4^{3-}/\text{SO}_4^{2-}$  selectivity is likely due to surface fouling from organic matter (increasing mass transfer resistance to sites)<sup>21</sup> and competition with negatively charged natural organic matter for sites.<sup>33</sup> In

WBA, relatively constant  $\text{PO}_4^{3-}/\text{SO}_4^{2-}$  and  $\text{PO}_4^{3-}/\text{Cl}^-$  selectivity suggests no solution composition dependence (**Figure 5b**). The higher FeOnp distribution on the periphery of the WBA versus the core facilitates high phosphate removal (due to less intraparticle diffusion resistance). However, the remaining tertiary amine sites are less selective towards anions of different valence at the studied pH, particularly distinguishing between mono and divalent anions.<sup>17</sup> Furthermore, the chloride leaching in WBA leads to a negative selectivity compared to SBA. Similar trends are observed at a 0.9 g/L resin dose (**Figure S29**).

### 3.5.2 Effect of Organic Matter on Phosphate Adsorption

Real wastewater contains a variety of organic matter (OM) species that can impact adsorption performance.<sup>34,35</sup> Using complementary aqueous- phase and solid- state analysis methods, we aimed to investigate and quantify the role of organic matter in phosphate adsorption (**Figure 6**). TOC analysis quantified organic matter adsorption (**Figure 6a**), while aqueous phosphate analysis evaluated phosphate adsorption in synthetic wastewater solutions with and without organic matter (**Figure 6b**). All other components are at the same solution concentration in SWW and SWW + OM, so the only difference is the addition of the organic matter.

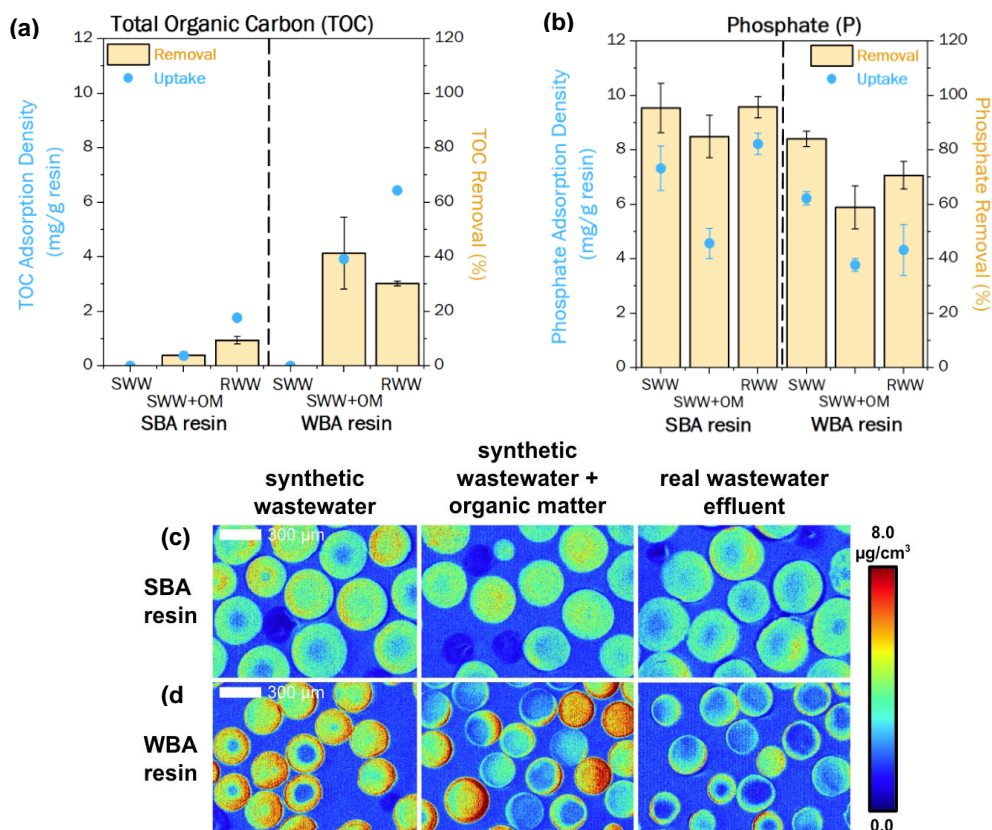


**Figure 6. Influence of organic matter on phosphate adsorption.** (a) TOC analysis and (b) phosphate adsorption for SBA and WBA across solution with no organic matter (simulated wastewater) and solutions with organic matter (simulated wastewater with organic matter and real wastewater). Dashed line separates the SBA and WBA values. (c,d) XRF of P with simulated wastewater, simulated wastewater with organic matter, and real wastewater (RWW) for SBA and WBA.

As expected, we observed a reduced phosphate adsorption capacity in solutions with organic matter due to competitive adsorption. Specifically, we observed a difference in phosphate adsorption between synthetic wastewater with and without organic matter for SBA and WBA ( $p$ -value =  $2 \times 10^{-3}$  and  $< 1 \times 10^{-5}$ , respectively). At the studied pH values, organic matter is negatively charged and therefore attracted to the ammonium moieties, affecting the phosphate adsorption density.<sup>36</sup> Further, organic matter can complex with iron oxides even at circumneutral pH resulting in a decrease in phosphate adsorption.<sup>37,38</sup> The XRF maps show a reduction (from approximately 8 to 4  $\mu\text{g}/\text{cm}^2$ ) in phosphate distribution on the resin periphery after adsorption in solutions containing organic matter, suggesting adsorption of organic matter on both resin types restricts phosphate adsorption (**Figure 6c,d**). Compared to SBA, WBA exhibited a higher TOC removal and adsorption due to the negatively charged natural organic matter (NOM) at this pH, which preferentially adsorbs to WBA through ion exchange.<sup>39</sup> Additionally, the greater hydrophilicity of TOC, combined with a higher affinity for hydrophilic compounds of WBA due to the greater charge density of its protonated secondary amino sites compared to the quaternary ammonium sites of SBA,<sup>40</sup> further enhances its removal efficiency. Observed trends with a 0.9 g/L resin dose were similar to those described for 2 g/L (**Figure S30**).

## Conclusions

In this study, we developed a quantitative solid-state characterization method that complements conventional aqueous analysis of resins for nutrient recovery from wastewaters. We observed differences in iron speciation and penetration, resultant phosphate distribution, and adsorption capacity and selectivity between SBA and WBA resin types, several of which are attributed to the lower porosity and likely lower crosslinking of the WBA resin. Both goethite and ferrihydrite iron phases were observed in the SBA and WBA resins, but the SBA resin contained primarily goethite, while WBA was more ferrihydrite abundant. The speciation of iron nanoparticles in the resin matrix has implications for long-term performance because it influences adsorption capacity, binding behavior and stability. By modifying the functionalization procedure (i.e., tuning the pH, reaction time), we can limit the conversion of ferrihydrite to goethite which can enhance phosphate adsorption capacity and selectivity. However, the higher reactivity and amorphous nature of ferrihydrite make it metastable, potentially reducing its long-term stability in the polymeric matrix.<sup>41</sup> Therefore, optimizing the Fe-phase composition is key to designing a material with enhanced stability and adsorption performance. We also observed and quantified phosphorus distribution changes in the presence of competing ions and organic matter. The distribution of phosphate was more heterogeneous for WBA, due to the lower porosity and high concentration of iron sites around the periphery. With these insights, the efficiency of WBA can be further enhanced by selecting a polymeric matrix with higher porosity and utilizing Fe(II) precursors, which can reduce the rate of iron

(oxy)hydroxide precipitation compared to the  $\text{FeCl}_3$  currently used for functionalization, enabling Fe to penetrate deeper into the resin bead. Characterization of phosphorus speciation demonstrated its selective binding to the FeOnp sites. Notably, the adsorption density measured by solid-state, synchrotron-based techniques aligned closely with that from conventional aqueous analysis, supporting the use of applying these methods to visualize and quantify adsorption mechanisms within separation materials.

There are several limitations of this study that will be addressed in future work, including: (1) our inability to differentiate between phosphate binding to goethite vs. ferrihydrite due to difficulty differentiating the pre-edge feature of the XANES spectra; (2) a lack of characterization of the complexes formed with organic matter, which was beyond the scope of this study; (3) the use of acetic acid as a model compound for organic matter, which may not fully capture all possible organic interactions with resins; and (4) only evaluating one synthetic and real wastewater type. Additionally, we did not explore whether changes to the WBA functionalization procedure could lead to homogeneous iron distribution.

There are also several extensions of this study that can be addressed in future work. The methods we established here can be expanded to apply to (1) regeneration methods and (2) other adsorbates (e.g., ammonia). Electrochemical regeneration can circumvent the greenhouse gas emissions associated with conventional commercial base regeneration,<sup>42</sup> and synchrotron-enable characterization can enhance understanding of regeneration mechanisms. Future nutrient recovery technologies need to align with practical applications;<sup>43</sup> thus, we will explore the tandem recovery of ammonium and phosphate within a single system to enable product fertilizer precipitation (e.g., struvite when paired with  $\text{Mg}^{2+}$  or hydroxyapatite when paired with  $\text{Ca}^{2+}$ ). By understanding the binding mechanism of selective phosphate adsorption and validating solid-state characterization as a complement to aqueous characterization, this study provides a fundamental foundation for designing sustainable systems for phosphate removal and recovery.

## ASSOCIATED CONTENT

### SUPPORTING INFORMATION

Supporting information includes historical trends of global phosphorus mining, phosphate speciation as a function of pH, speciation of hydrated iron oxides as a function of pH, composition of wastewaters, difference in phosphate adsorption performance between resins, scanning electron microscopy (SEM) images of resins, phosphate selectivity analyses, quantitative analysis of sulfate adsorption from XRF mapping, and kinetic profiles for phosphate, sulfate, and chloride adsorption. This material is available free of charge via the Internet at <http://pubs.acs.org>.

### AUTHOR INFORMATION

## Corresponding Author

William Tarpeh, [wtarpeh@stanford.edu](mailto:wtarpeh@stanford.edu), 443 Via Ortega, Room 387, Stanford, CA, 94305, United States

## Author Contributions

The manuscript was written through contributions of all authors. / All authors have given approval to the final version of the manuscript. / ‡These authors contributed equally.

## ACKNOWLEDGMENT

Funding for this work was made possible by the National Alliance for Water Innovation (NAWI) which is supported by the U.S. Department of Energy, Energy Efficiency and Renewable Energy Office, Advanced Manufacturing Office under Funding Opportunity Announcement DE-FOA-0001905. Funding has been provided in full or in part through an agreement with the California State Water Resources Control Board using funds from Proposition 1. The contents of this document do not necessarily reflect the views and policies of the foregoing, nor does mention of trade names or commercial products constitute endorsement or recommendation for use.

Use of the Stanford Synchrotron Radiation Lightsource at the SLAC National Accelerator Laboratory, is supported by the US Department of Energy, Office of Science, Office of Basic Energy Sciences under Contract No. DE-AC02-76SF00515. Part of this work was performed at the Stanford Nano Shared Facilities (SNSF), supported by the National Science Foundation under award ECCS-2026822.

N.S. acknowledges funding support from the Stanford Doerr School of Sustainability Accelerator E.A. was supported through the National Science Foundation Graduate Research Fellowship (Grant No. 1656518). D.B. was supported by the Stanford University Vice Provost for Undergraduate Education through the Chemical Engineering Research Experience for Undergraduates program. We thank Eleanor Spielman-Sun, Sam Webb, Brandon Clark, and Victoria Yang for their help conducting beamtime experiments. We thank Dr. Ludmilla Aristilde for providing XANES spectra of phosphate adsorbed to goethite and ferrihydrite for speciation analysis. We thank Dr. Taigyu Joo for his help with SEM preparation and imaging.

## ABBREVIATIONS

HAIX, hybrid anion exchange resin; NOM, natural organic matter; OM, organic matter; RWW, real wastewater; TOC, total organic carbon; SBA, strong base anion exchange resin; SWW, synthetic wastewater; WBA, weak base anion exchange resin;  $\mu$ -XRF, micro-X-ray fluorescence; and  $\mu$ -XANES, micro-X-ray adsorption near-edge spectroscopy.

## REFERENCES

- (1) Desmidt, E.; Ghyselbrecht, K.; Zhang, Y.; Pinoy, L.; Van der Bruggen, B.; Verstraete, W.; Rabaey, K.; Meesschaert, B. Global Phosphorus Scarcity and Full-Scale P-Recovery Techniques: A Review. *Critical Reviews in Environmental Science and Technology* **2015**, *45* (4), 336–384.
- (2) Snyder, N. A.; Morales-Guio, C. G. Perspective on the Electrochemical Recovery of Phosphate from Wastewater Streams. *Electrochemical Science Adv* **2022**.
- (3) USGS. *Phosphate Rock Mineral Commodities Summary*; USGS, 2023.
- (4) Approaching Peak Phosphorus. *Nat. Plants* **2022**, *8* (9), 979–979.
- (5) Mayer, B. K.; Baker, L. A.; Boyer, T. H.; Drechsel, P.; Gifford, M.; Hanjra, M. A.; Parameswaran, P.; Stoltzfus, J.; Westerhoff, P.; Rittmann, B. E. Total Value of Phosphorus Recovery. *Environ. Sci. Technol.* **2016**, *50* (13), 6606–6620.
- (6) Jones, E. R.; van Vliet, M. T. H.; Qadir, M.; Bierkens, M. F. P. Country-Level and Gridded Estimates of Wastewater Production, Collection, Treatment and Reuse. *Earth System Science Data* **2021**, *13* (2), 237–254.
- (7) Apraku, E.; Farmer, M.; Lavallais, C.; Soriano, D. A.; Notestein, J.; Tyo, K.; Dunn, J.; Tarpeh, W. A.; Wells, G. F. Toward a Circular Nitrogen Bioeconomy: Integrating Nitrogen Bioconcentration, Separations, and High-Value Products for Nitrogen Recovery. *Current Opinion in Biotechnology* **2025**, *91*, 103225.
- (8) Zheng, Y.; Wan, Y.; Zhang, Y.; Huang, J.; Yang, Y.; Tsang, D. C. W.; Wang, H.; Chen, H.; Gao, B. Recovery of Phosphorus from Wastewater: A Review Based on Current Phosphorous Removal Technologies. *Crit Rev Environ Sci Technol* **2022**, *53* (11), 1148–1172.
- (9) Clark, B.; Sharma, N.; Apraku, E.; Dong, H.; Tarpeh, W. A. Ligand Exchange Adsorbents for Selective Phosphate and Total Ammonia Nitrogen Recovery from Wastewaters. *Acc. Mater. Res.* **2024**, *5* (4), 492–504.
- (10) Sharma, N.; Apraku, E.; Gong, M.; Tarpeh, W. A. Integrating Adsorbents and Electrochemistry to Advance Selective Wastewater Phosphate Separations. *Current Opinion in Chemical Engineering* **2025**, *47*, 101080.
- (11) Kroiss, H.; Rechberger, H.; Egle, L.; Kroiss, H.; Rechberger, H.; Egle, L. *Phosphorus in Water Quality and Waste Management*; IntechOpen, 2011.
- (12) Dong, H.; Wei, L.; Tarpeh, W. A. Electro-Assisted Regeneration of PH-Sensitive Ion Exchangers for Sustainable Phosphate Removal and Recovery. *Water Research* **2020**, *184*, 116167.
- (13) Blaney, L. M.; Cinar, S.; SenGupta, A. K. Hybrid Anion Exchanger for Trace Phosphate Removal from Water and Wastewater. *Water Research* **2007**, *41* (7), 1603–1613.
- (14) Dong, H.; Wu, Z.; Liu, M. J.; Tarpeh, W. A. The Role of Intraparticle Diffusion Path Length during Electro-Assisted Regeneration of Ion Exchange Resins: Implications for Selective Adsorbent Design and Reverse Osmosis Pretreatment. *Chemical Engineering Journal* **2021**, *407*, 127821.



- (15) A. Tarpeh, W.; Wald, I.; Wiprächtiger, M.; L. Nelson, K. Effects of Operating and Design Parameters on Ion Exchange Columns for Nutrient Recovery from Urine. *Environ. Sci. Water Res. Technol.* **2018**, *4* (6), 828–838.
- (16) Bagastyo, A. Y.; Anggrainy, A. D.; Khoiruddin, K.; Ursada, R.; Warmadewanthi, I.; Wenten, I. G. Electrochemically-Driven Struvite Recovery: Prospect and Challenges for the Application of Magnesium Sacrificial Anode. *Separation and Purification Technology* **2022**, *288*, 120653.
- (17) SenGupta, A. K. *Ion Exchange in Environmental Processes: Fundamentals, Applications and Sustainable Technology*; John Wiley & Sons, Inc.: Hoboken, New Jersey, 2017.
- (18) Cumbal, L.; SenGupta, A. K. Arsenic Removal Using Polymer-Supported Hydrated Iron(III) Oxide Nanoparticles: Role of Donnan Membrane Effect. *Environ. Sci. Technol.* **2005**, *39* (17), 6508–6515.
- (19) Rousseau, R. W. *Handbook of Separation Process Technology*; A Wiley-Interscience publication; Wiley, 1987.
- (20) Tewari, P. H.; Lee, W. Adsorption of Co(II) at the Oxide-Water Interface. *Journal of Colloid and Interface Science* **1975**, *52* (1), 77–88.
- (21) Niemann, V. A.; Huck, M.; Steinrück, H.-G.; Toney, M. F.; Tarpeh, W. A.; Bone, S. E. X-Ray Absorption Spectroscopy Reveals Mechanisms of Calcium and Silicon Fouling on Reverse Osmosis Membranes Used in Wastewater Reclamation. *ACS EST Water* **2023**, *3* (8), 2627–2637.
- (22) Bone, S. E.; Steinrück, H.-G.; Toney, M. F. Advanced Characterization in Clean Water Technologies. *Joule* **2020**, *4* (8), 1637–1659.
- (23) Foster, X.; Vaneekhaute, C. Modifying the Resin Type of Hybrid Anion Exchange Nanotechnology (HAIX-Nano) to Improve Its Regeneration and Phosphate Recovery Efficiency. *npj Clean Water* **2021**, *4* (1), 1–8.
- (24) Webb, S. M. The MicroAnalysis Toolkit: X-ray Fluorescence Image Processing Software. *AIP Conference Proceedings* **2011**, *1365* (1), 196–199.
- (25) Ravel, B.; Newville, M. ATHENA, ARTEMIS, HEPHAESTUS: Data Analysis for X-Ray Absorption Spectroscopy Using IFEFFIT. *J Synchrotron Rad* **2005**, *12* (4), 537–541.
- (26) Liu, Y.; Meirer, F.; Williams, P. A.; Wang, J.; Andrews, J. C.; Pianetta, P. TXM-Wizard: A Program for Advanced Data Collection and Evaluation in Full-Field Transmission X-Ray Microscopy. *Journal of Synchrotron Radiation* **2012**, *19* (2).
- (27) Belloni, C.; Korving, L.; Witkamp, G. J.; Brück, E.; de Jager, P.; Dugulan, A. I. FeOOH and (Fe,Zn)OOH Hybrid Anion Exchange Adsorbents for Phosphate Recovery: A Determination of Fe-Phases and Adsorption–Desorption Mechanisms. *Chemical Engineering Journal* **2023**, *473*, 145287.
- (28) Bao, T.; Damtie, M. M.; Wang, C. Y.; Li, C. L.; Chen, Z.; CHO, K.; Wei, W.; Yuan, P.; Frost, R. L.; Ni, B.-J. Iron-Containing Nanominerals for Sustainable Phosphate Management: A Comprehensive Review and Future Perspectives. *Science of The Total Environment* **2024**, *926*, 172025.
- (29) Farcas, F. E.; Lothenbach, B.; Mundra, S.; Borca, C. N.; Albert, C. C.; Isgor, O. B.; Huthwelker, T.; Angst, U. M. Transformation of 2-Line Ferrihydrite to Goethite at Alkaline PH. *Environ. Sci. Technol.* **2023**, *57* (42), 16097–16108.
- (30) Schwertmann, U. Solubility and Dissolution of Iron Oxides. *Plant Soil* **1991**, *130* (1), 1–25.
- (31) Anatolievich Sochilin, Vladimir. AMINATED ION EXCHANGE RESINS AND PRODUCTION METHODS THEREOF. US 8,822,554 B2.
- (32) Khare, N.; Martin, J. D.; Hesterberg, D. Phosphate Bonding Configuration on Ferrihydrite Based on Molecular Orbital Calculations and XANES Fingerprinting. *Geochimica et Cosmochimica Acta* **2007**, *71* (18), 4405–4415.
- (33) Boyer, T. H.; Singer, P. C.; Aiken, G. R. Removal of Dissolved Organic Matter by Anion Exchange: Effect of Dissolved Organic Matter Properties. *Environ. Sci. Technol.* **2008**, *42* (19), 7431–7437.
- (34) Apraku, E.; Laguna, C. M.; Wood, R. M.; Sharma, N.; Dong, H.; Tarpeh, W. A. Enhancing Resource Recovery through Electro-Assisted Regeneration of an Ammonia-Selective Cation Exchange Resin. *ACS EST Water* **2024**, *4* (10), 4521–4532.
- (35) Haddad, M.; Oie, C.; Vo Duy, S.; Sauvé, S.; Barbeau, B. Adsorption of Micropollutants Present in Surface Waters onto Polymeric Resins: Impact of Resin Type and Water Matrix on Performance. *Science of The Total Environment* **2019**, *660*, 1449–1458.
- (36) Newcombe, G. Charge vs. Porosity — Some Influences on the Adsorption of Natural Organic Matter (NOM) by Activated Carbon. *Water Science and Technology* **1999**, *40* (9), 191–198.
- (37) Weng, L.; Van Riemsdijk, W. H.; Hiemstra, T. Adsorption of Humic Acids onto Goethite: Effects of Molar Mass, PH and Ionic Strength. *Journal of Colloid and Interface Science* **2007**, *314* (1), 107–118.
- (38) Yang, Y.; Lohwacharin, J.; Takizawa, S. Analysis of Adsorption Processes of Dissolved Organic Matter (DOM) on Ferrihydrite Using Surrogate Organic Compounds. *Environ Sci Pollut Res* **2017**, *24* (27), 21867–21876.
- (39) Laforce, E.; Stals, I.; Cornelissen, E. R.; Vermeir, P.; De Clercq, J. Revealing the Effect of Anion Exchange Resin Conditioning on the PH and Natural Organic Matter Model Compounds Removal Mechanisms. *Journal of Environmental Chemical Engineering* **2022**, *10* (5), 108315.
- (40) Bolto, B.; Dixon, D.; Eldridge, R.; King, S.; Linge, K. Removal of Natural Organic Matter by Ion Exchange. *Water Research* **2002**, *36* (20), 5057–5065.

- (41) Pan, B.; Chen, D.; Zhang, H.; Wu, J.; He, F.; Wang, J.; Chen, J. Stability of Hydrous Ferric Oxide Nanoparticles Encapsulated inside Porous Matrices: Effect of Solution and Matrix Phase. *Chemical Engineering Journal* **2018**, *347*, 870–876.
- (42) Kavvada, O.; Tarpeh, W. A.; Horvath, A.; Nelson, K. L. Life-Cycle Cost and Environmental Assessment of Decentralized Nitrogen Recovery Using Ion Exchange from Source-Separated Urine through Spatial Modeling. *Environ. Sci. Technol.* **2017**, *51* (21), 12061–12071.
- (43) Kogler, A.; Farmer, M.; Simon, J. A.; Tilmans, S.; Wells, G. F.; Tarpeh, W. A. Systematic Evaluation of Emerging Wastewater Nutrient Removal and Recovery Technologies to Inform Practice and Advance Resource Efficiency. *ACS EST Eng.* **2021**, *1* (4), 662–684.

